

Hydrogen bond topology and the ice VII/VIII and Ih/XI proton ordering phase transitions

Chris Knight,^{1,*} Sherwin J. Singer,^{1,†} Jer-Lai Kuo,^{2,‡} Tomas K. Hirsch,^{3,§} Lars Ojamäe,^{4,||} and Michael L. Klein^{5,¶}

¹Department of Chemistry, Ohio State University, Columbus, Ohio 43210, USA

²School of Physical and Mathematical Sciences, Nanyang Technological University, Singapore 637616

³Physical Chemistry, Arrhenius Laboratory, Stockholm University, SE-106 91 Stockholm, Sweden

⁴Department of Chemistry, IFM, Linköping University, SE-581 83 Linköping, Sweden

⁵Center for Molecular Modeling, University of Pennsylvania, Philadelphia, Pennsylvania 19104, USA

(Received 5 January 2006; published 16 May 2006)

Ice Ih, ordinary ice at atmospheric pressure, is a proton-disordered crystal that when cooled under special conditions is believed to transform to ferroelectric proton-ordered ice XI, but this transformation is still subject to controversy. Ice VII, also proton disordered throughout its region of stability, transforms to proton-ordered ice VIII upon cooling. In contrast to the ice Ih/XI transition, the VII/VIII transition and the crystal structure of ice VIII are well characterized. In order to shed some light on the ice Ih proton ordering transition, we present the results of periodic electronic density functional theory calculations and statistical simulations. We are able to describe the small energy differences among the innumerable H-bond configurations possible in a large simulation cell by using an analytic theory to extrapolate from electronic DFT calculations on small unit cells to cells large enough to approximate the thermodynamic limit. We first validate our methods by comparing our predictions to the well-characterized ice VII/VIII proton ordering transition, finding agreement with respect to both the transition temperature and structure of the low-temperature phase. For ice Ih, our results indicate that a proton-ordered phase is attainable at low temperatures, the structure of which is in agreement with the experimentally proposed ferroelectric Cmc_2 structure. The predicted transition temperature of 98 K is in qualitative agreement with the observed transition at 72 K on KOH-doped ice samples.

DOI: [10.1103/PhysRevE.73.056113](https://doi.org/10.1103/PhysRevE.73.056113)

PACS number(s): 64.60.Cn, 02.10.Ox

I. INTRODUCTION

In 1935, Pauling [1] predicted that there were $(3/2)^N$ different ways to arrange the hydrogen bonds (H bonds) of N water molecules in an ice Ih lattice, “ordinary ice,” subject to the ice rules. The ice rules state that each oxygen must be covalently bonded to two hydrogen atoms, there is only one hydrogen atom per bond, and each water molecule accepts a maximum of two hydrogen atoms from other waters, as illustrated in Fig. 1. The following year, Giauque and Stout measured the entropy of ice Ih near 0 K to be $Nk_B \ln \frac{3}{2}$ within experimental error [2]. Pauling’s estimate proved to be remarkably accurate and was verified when the exact result was calculated to be 1.5069^N [3]. This nonzero entropy implies that somewhere between freezing and 0 K, ordinary ice becomes a proton glass with a quenched, nearly random, arrangement of H bonds. There has been continued debate and research as to whether the H-bond arrangements are truly random, whether a phase transition to a fully proton-ordered structure exists, and if so, the identity of that structure.

Close to the melting point of ice, the protons are fully disordered subject to the ice rules. As ice is cooled to low

temperatures, proton motion comes to a halt, and a glassy transition has been observed to occur near 110 K [4], prohibiting the transition to a proton-ordered phase. As tabulated in Ref. [5], numerous dielectric studies of powder and single-crystal samples have been performed over the years. Kawada and Niinuma reported results of dielectric studies of single crystals with a Curie-Weiss temperature of 46 K and 55 K for H₂O [6,7] and D₂O [8], respectively, with the electric field parallel to the c axis. Studies by Johari and Whalley on powdered samples of H₂O indicate a Curie-Weiss tempera-

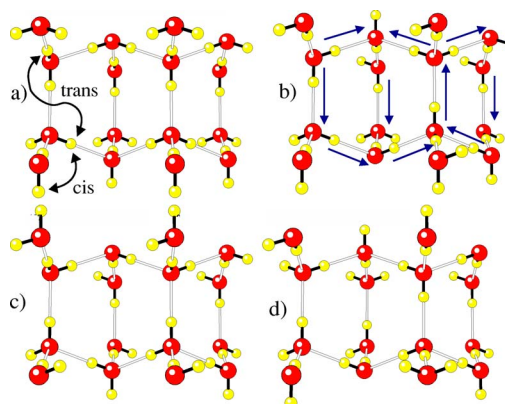


FIG. 1. (Color online) Four possible arrangements of H bonds within a 16-water-molecule $2 \times 1 \times 1$ orthorhombic unit cell of ice Ih. Here, *cis* and *trans* bonds are defined as whether protons lie on the same or opposite side of the H bond respectively, as indicated for isomer (a). The H-bond isomers are summarized mathematically by directed graphs in which directional bonds point from H-bond donor to H-bond acceptor, as illustrated for the isomer (b).

*Electronic address: cknight@chemistry.ohio-state.edu

†Electronic address: singer@chemistry.ohio-state.edu

‡Electronic address: jlkuo@ntu.edu.sg

§Present address: Stanford Linear Accelerator Center, Menlo Park, CA 94025. Electronic address: tompa@slac.stanford.edu

||Electronic address: lars@ifm.liu.se

¶Electronic address: klein@lrsm.upenn.edu

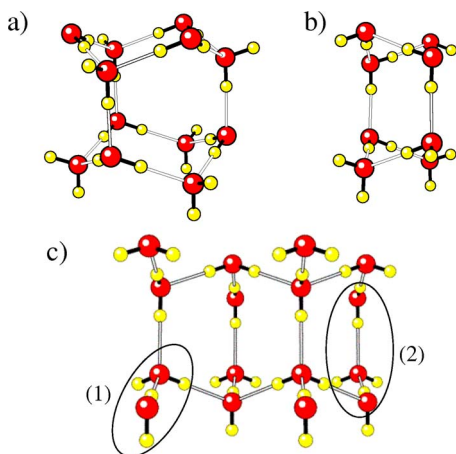


FIG. 2. (Color online) (a) A $1 \times 1 \times 1$ hexagonal unit cell of ice Ih, space group $P6_3/mmc$, containing 12 water molecules. (b) A $1 \times 1 \times 1$ orthorhombic unit cell of ice Ih, space group $Cmc2_1$, containing 8 water molecules. Bonds that appear to point straight up and down are parallel to the c axis and hence called c -axis bonds. The remaining bonds, perpendicular to the c axis, are referred to as ab bonds. (c) Proposed experimental structure of proton ordered ice Ih, ice XI, as determined from diffraction and thermal depolarization experiments [13–18]. The ab -layer bonds (1) are all *cis* with the ab layers polarized parallel to the b axis and alternating layers oppositely aligned. The c -axis bonds (2) are *trans* and all oriented in the same direction. *cis* and *trans* H bonds are defined, respectively, as to whether the non-hydrogen-bonded hydrogen atoms fall on the same or opposite side of the H bond.

ture significantly lower, 6.2 K [5]. However, in samples doped with impurities, particularly KOH, it was observed that there is a clear calorimetric signature of a first-order phase transition at 72 K with a weak dependence on the concentration of the KOH impurity [8,9]. In experiments with samples of D_2O , the transition temperature is shifted by 4° and occurs at 76 K. Antarctic ice samples have been examined with neutron diffraction and Raman spectroscopy. It is believed that these samples, kept at a constant low temperature for thousands of years, have equilibrated to a proton-ordered arrangement [10]. Those studies indicate that a second-order phase transition to an H-bond-ordered phase of ice occurs at 237 K, which is significantly larger than the observed transition temperature in KOH-doped ice samples. Neutron diffraction spectra of Greenland ice samples, prepared under similar conditions, showed no distinct differences when compared to the spectra of ice Ih, thus casting doubt on the earlier Antarctic studies [11]. Additional diffraction studies of Antarctic ice samples concur that it is unlikely to observe a proton-ordered arrangement under such conditions [12].

The unit cell of ice Ih, Fig. 2, is hexagonal with space group $P6_3/mmc$. The symmetry of the low-temperature proton-ordered configuration, ice XI, shown in Fig. 2(c), is orthorhombic, space group $Cmc2_1$, as indicated by neutron scattering [13–16] and thermal depolarization experiments [17,18] on KOH-doped ice Ih. Bonds that are oriented parallel to the c axis all point in the same direction. The ab layers, composed of bonds oriented perpendicular to the c axis, are polarized parallel to the b axis with alternating lay-

ers oppositely aligned. Thus, the structure is overall antiferroelectric in the a and b directions and ferroelectric in the c direction. This antiferroelectric arrangement of the ab layers gives rise to a slight displacement of the oxygen lattice parallel to the b axis in the direction of the polarization. The calculated shift, 0.11 Å, determined from the optimized geometry of the ice XI configuration, calculated as described below, is in agreement with the experimentally determined shift of 0.12 Å [13].

This view has been contested: Iedema *et al.* [19] referred to more recent claims as “UFI citations (underidentified ferroelectric ices) in the literature.” Even if the $Cmc2_1$ structure proves to be correct, there is some justification for characterizing the current state of knowledge of low-temperature ice Ih/XI as “underidentified.” While a mechanism has been proposed for incomplete conversion of ice Ih to ice XI [20], several features of the presumed ice Ih/XI transition are not understood: While the calorimetric signature of the Ih/XI transition is remarkably insensitive to KOH concentration, the amount of conversion, as measured by the total heat of transformation, is strongly concentration dependent. If KOH truly acts as a catalyst and samples have adequate time to equilibrate, there should be no concentration dependence. The KOH seems to be playing another role, perhaps related to the crystal strain discussed by Johari [20]. Furthermore, there are reports that protons in ice become immobile below a certain temperature due to being trapped by the defects present in ice [21]. Wooldridge and Devlin performed Fourier-transform (FT) IR experiments which indicated that proton motion comes to a halt below 100 K [22]. More recently, “soft-landing” experiments by Cowin *et al.* indicate that hydronium ions are in fact immobile at all temperatures below 190 K [23]. If hydroxide is as immobile as excess protons at low temperature, then the basis for the catalytic role of hydroxide would be thrown in doubt. Recent dielectric and calorimetric experiments [24] indicate that the alkali hydroxide dopants polarize nearby water molecules to promote orientational ordering at low temperatures which may explain the observed weak concentration dependence on the amount of transformation achieved.

In contrast to the controversy surrounding the ice Ih/XI proton ordering phase transition, the ice VII/VIII transition has been well characterized. The ice VII/VIII proton ordering transition will then serve as a means for validating our theoretical methods. Ice VII was first identified by Bridgman [25] in 1937. Ice VII has one of the simplest structures out of all the high-pressure phases of ice, two interpenetrating, but not interconnected ice Ic lattices. The unit cell of the ice VII crystal is cubic, space group $Pn3m$, containing two water molecules. X-ray [26,27] and neutron [28] diffraction studies indicate that the H bonds in ice VII, the structure of which is shown below in Fig. 5, are fully disordered subject to the ice rules. Ice VIII is the corresponding low-temperature proton-ordered structure. The ice VIII unit cell is tetragonal, space group $I4_1/amd$, containing eight water molecules. Both sublattices are ferroelectrically aligned parallel to the c axis, but the sublattices are oriented opposite to one another, resulting in an overall antiferroelectric structure. The relative oxygen positions remain essentially unchanged from that of ice VII structure except for a small distortion, ~ 0.2 Å [29–31], aris-

ing from the nonbonded oxygen-oxygen interactions between the sublattices.

The ice VII/VIII proton ordering transition was first observed when dielectric experiments indicated that the Debye relaxation disappeared below 0 °C [32]. Over a range of pressures from 2.1 to 12 GPa, proton ordering, via rearrangement of H bonds, occurs at nearly constant temperature. All experiments are in general agreement on the ice VII/VIII transition temperature, 263–273 K [28,33], although hysteresis [34] effects make the precise determination difficult. The effects of D₂O on the transformation are negligible at these temperatures, shifting on the order of a degree [35], indicating that quantum effects are minimal. In the ice Ih-XI transition, the transition temperature shifts from 72 K for H₂O to 76 K for D₂O. With still higher pressure, the ice VII/VIII transition temperature abruptly decreases as the mechanism of the transition shifts to proton tunneling across the shortened H bonds. Our calculations are pertinent to the temperature-independent region.

Predictions of H-bond ordering in ice encounter several obstacles. Buch, Sandler, and Sadlej [36] showed that commonly used empirical potentials disagree among each other with regard to the subtle energetic ordering of the H-bond isomers in ice Ih and by an order of magnitude with respect to the range of energy differences. Furthermore, none of the empirical potentials predicted the ground state to be the *Cmc*2₁ crystal structure, Fig. 2, suggested by diffraction data, including a potential they constructed with that hope in mind. We overcome the problem of determining H-bond energetics via electronic density-functional-theory (DFT) calculations. Below, we report results from three DFT methods that yield consistent results for the relative energetics of H-bond isomers, including the identification of the ground state. In the future, empirical potentials capable of describing the energetics of H-bond isomers in ice may be available. Even if that goal is realized, it is useful to have a method in which the construction of empirical potentials is entirely circumvented. The data presented in this work provide a benchmark by which future empirical potentials can be calibrated.

While it may be feasible to perform electronic structure calculations on a handful of H-bond isomers for a small unit cell, it would certainly be impractical to perform the same level of calculation on the $\sim \binom{3}{2}^N$ H-bond isomers of a unit cell large enough to obtain good statistics. We solve the problem of the statistical sampling of H-bond configurations by linking energy to hydrogen-bond topology using graph invariants [37–41], combinations of H-bond variables which are invariant to symmetry operations of the appropriate space group and are therefore appropriate variables for describing scalar physical properties. Graph invariants provide a means to “bootstrap” from expensive DFT calculations for smaller unit cells to statistical mechanics simulations using a larger unit cell.

This report is a comprehensive account following an earlier Letter [40] and is organized as follows. In Sec. II, we gently introduce the graph techniques we use to link hydrogen-bond topologies to scalar physical quantities. A more detailed account can be found in previous works [38,39]. Graph invariants are then validated, in Sec. III, as an appropriate method of treating H-bond fluctuations in a large

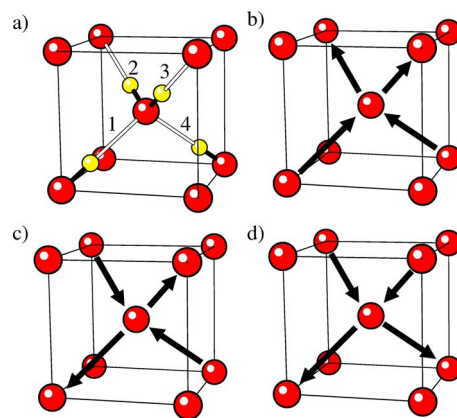


FIG. 3. (Color online) (a) An isomer of a two-water-molecule primitive unit cell of ice VII, obeying the Bernal-Fowler ice rules, is shown. The thin black lines outline the unit cell and neighboring oxygen atoms are included for clarity. The orientations of H bonds in this isomer are assigned to be the canonical arrangement of H bonds. The H bonds are labeled from 1 to 4 to provide a means to associate a bond variable, b_r , with each H-bond labeled r . (b) The H-bond configuration in (a) is summarized by a directed graph. The H bonds are taken to point from oxygen donor to oxygen acceptor as discussed in the text. (c) and (d) Additional directed graphs corresponding to other H-bond isomers of ice VII that satisfy the Bernal-Fowler ice rules and periodicity constraints. As an example, if all the bond variables b_r for configuration (b) were assigned the value +1, then all the b_r 's for configuration (d) would take the value -1 since all H bonds are reversed.

simulation cell by direct comparison to experimental data on the proton ordering transition in the ice VII/VIII system. In Sec. IV, we discuss the agreement among various DFT methods in describing the energetics of H-bond isomers for two unit cells of ice Ih and present the results of statistical simulations on the ice Ih/XI proton ordering phase transition.

II. INTRODUCTION TO GRAPH INVARIANTS FOR ICE

Each hydrogen bond in ice consists of a single hydrogen atom covalently bonded to one oxygen atom from the donor molecule and hydrogen bonded to a second oxygen atom from the acceptor molecule. Hence, H bonds are directional and conventionally taken to point from donor to acceptor, as shown in Fig. 3. The H-bond network can then be summarized mathematically by oriented graphs, vertices connected by directed lines. The direction of the r th H bond in the ice lattice is specified by a bond variable b_r , which takes values ± 1 according to whether the bond points along, or opposite to, an arbitrarily defined canonical direction for that bond. The directed graph of Fig. 3(b) defines our canonical orientation of the H bonds in the two-water-molecule primitive unit cell of ice VII. The bond variables b_1 , b_2 , b_3 , and b_4 for one of the actual H-bond isomers of ice VII are assigned the value of +1 when they point in the directions shown in Fig. 3(b) and -1 when they point in the opposite direction. Examples of directed graphs for the two-water-molecule unit cell of ice VII are shown in the bottom of Fig. 3.

Some graphs or their corresponding H-bond isomers may be related to others by one or more symmetry operations, such as rotations, reflections, and translations. In this simple exercise using the highly symmetric unit cell of ice VII, it so happens that all H-bond configurations of this primitive unit cell, obeying the ice rules and periodicity constraints, are related to every other graph via symmetry operations of the corresponding symmetry group, space group $Pn3m$ for ice VII, and thus there is only one symmetry distinct H-bond configuration. Therefore, scalar properties, such as energy, should be equivalent for all H-bond configurations allowed in this unit cell. In larger unit cells, the possible graphs can be partitioned into sets (orbits) of symmetry-related configurations. All scalar physical properties, such as the energy, must be identical for all configurations within a set. If energy depends on topological features of the H-bond configuration, then energy must depend on functions of bond variables b_r , which are themselves equivalent under symmetry operations [38,39].

Functions of bond variables, which are invariant to symmetry operations of the corresponding symmetry group, can be constructed via application of the projection operator for the totally symmetric representation. Application of the projection operator on a single-bond variable b_r yields

$$I_r = C_r \sum_{\alpha \in G} g_\alpha(b_r) = \frac{1}{|G|} \sum_{\alpha \in G} g_\alpha(b_r), \quad (1)$$

where C_r is a normalization constant, g_α is a symmetry element of the group G , and the sum is performed over all elements in the group G . The normalization constant C_r is chosen to be the inverse of the order of the group $|G|$, making the graph invariants intensive quantities. I_r is referred to as a first-order graph invariant constructed by application of the projection operator to bond r . For systems with sufficient symmetry, most first-order invariants may algebraically equal zero. A necessary and sufficient condition for any graph invariant to be identically zero is the existence of symmetry elements that take bond b_r into minus itself [38]:

$$g_\alpha(b_r) = -b_r. \quad (2)$$

Higher-order graph invariants I_{rs}, I_{rst}, \dots can be constructed as follows:

$$I_{rs} = \frac{1}{|G|} \sum_{\alpha \in G} g_\alpha(b_r b_s), \quad (3)$$

$$I_{rst} = \frac{1}{|G|} \sum_{\alpha \in G} g_\alpha(b_r b_s b_t), \dots, \quad (4)$$

where I_{rs} is a second-order graph invariant, I_{rst} is a third-order graph invariant, and so on. For the primitive cell of ice VII, all first-order invariants are identically zero. Application of the projection operator for the totally symmetric representation onto all pairs of bonds yields two unique second-order graph invariants

$$I_{1,1} = \frac{1}{4}(b_1^2 + b_2^2 + b_3^2 + b_4^2), \quad (5)$$

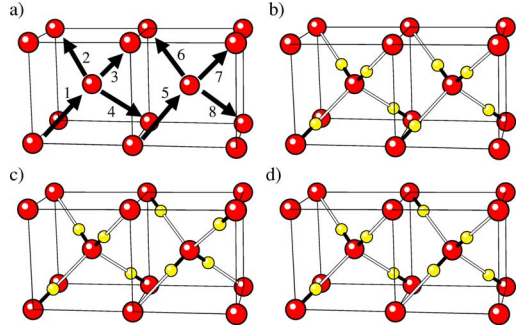


FIG. 4. (Color online) (a) The canonical orientation of H bonds, obeying the Bernal-Fowler ice rules, for a unit cell of ice VII measuring $2 \times 1 \times 1$ primitive cells on each side. The black lines outline the primitive unit cells, and neighboring oxygen atoms are included for clarity. H bonds are labeled so as to identify a bond variable b_r with H bond r . The orientations of H bonds in this isomer are assigned to be the canonical arrangement of H bonds, and all bond variables are assigned the value +1. (b)–(d) Isomers of three symmetry-distinct H-bond configurations possible in this unit cell. The bond variables for each of the three configurations, assigned according to H-bond configuration (a), are tabulated in Table I.

$$I_{1,2} = \frac{1}{6}(b_1 b_2 + b_1 b_3 + b_1 b_4 - b_2 b_3 - b_2 b_4 - b_3 b_4). \quad (6)$$

The action of the projection operator onto bond pairs $b_r b_s$ when $r=s$ yields Eq. (5) while all permutations of r and s such that $r \neq s$ yield Eq. (6). Evaluating the second-order graph invariants for the H-bond configurations in Fig. 3 yields $I_{1,1}=1$ and $I_{1,2}=0$ for all three configurations. The second-order invariant $I_{1,1}$ effectively counts the number of H bonds in the system, which evaluates to a constant for all H-bond configurations allowed by the ice rules and periodicity constraints. Since $I_{1,2}$ evaluates to zero for all possible H-bond configurations allowed in this primitive cell, both second-order invariants will have the same value for all H-bond isomers allowed by the ice rules and periodicity constraints, reflecting the fact that there is only one symmetry distinct H-bond isomer possible in the primitive unit cell of ice VII. A more interesting exercise, although still relatively simple, would be to analyze the invariants obtained from a unit cell of ice VII measuring $2 \times 1 \times 1$ primitive cells on each side as shown in Fig. 4. There are three symmetry-distinct isomers allowed in this unit cell. All first-order invariants for this cell are identically zero, and there are four unique second-order invariants

$$I_{1,1} = \frac{1}{8}[b_1 b_1 + b_2 b_2 + b_3 b_3 + b_4 b_4 + b_5 b_5 + b_6 b_6 + b_7 b_7 + b_8 b_8], \quad (7)$$

$$I_{1,2} = \frac{1}{24}[2b_1 b_2 - 2b_3 b_4 + 2b_5 b_6 - 2b_7 b_8 + b_1 b_3 - b_2 b_3 + b_1 b_4 - b_2 b_4 + b_3 b_5 + b_4 b_5 - b_3 b_6 - b_4 b_6 + b_1 b_7 - b_2 b_7 + b_5 b_7 - b_6 b_7 + b_1 b_8 - b_2 b_8 + b_5 b_8 - b_6 b_8], \quad (8)$$

TABLE I. Bond variables and evaluated second-order invariants for the three symmetry-distinct H-bond isomers of the $2 \times 1 \times 1$ unit cell of ice VII. The bond variables are assigned the value of ± 1 depending on the orientation of the H bond with respect to the canonical orientation illustrated in Fig. 4(a). The last four columns indicate the values that the second-order graph invariants take when evaluated for each H-bond configuration.

Graph	b_1	b_2	b_3	b_4	b_5	b_6	b_7	b_8	$I_{1,1}$	$I_{1,2}$	$I_{1,5}$	$I_{1,6}$
(a),(b)	1	1	1	-1	1	1	1	-1	1	$\frac{1}{3}$	$\frac{1}{3}$	$-\frac{1}{3}$
(d)	1	1	1	-1	-1	-1	-1	1	1	$\frac{1}{3}$	$\frac{2}{3}$	0
(d)	1	1	1	-1	-1	-1	1	-1	1	$\frac{1}{3}$	1	$\frac{1}{3}$

$$I_{1,5} = \frac{1}{12} [b_1 b_5 + b_2 b_6 + b_3 b_7 + b_4 b_8 + b_1 b_1 + b_2 b_2 + b_3 b_3 + b_4 b_4 + b_5 b_5 + b_6 b_6 + b_7 b_7 + b_8 b_8], \quad (9)$$

$$I_{1,6} = \frac{1}{24} [2b_1 b_6 + 2b_2 b_5 - 2b_3 b_8 - 2b_4 b_7 + b_1 b_3 - b_2 b_3 + b_1 b_4 - b_2 b_4 + b_3 b_5 + b_4 b_5 - b_3 b_6 - b_4 b_6 + b_1 b_7 - b_2 b_7 + b_5 b_7 - b_6 b_7 + b_1 b_8 - b_2 b_8 + b_5 b_8 - b_6 b_8]. \quad (10)$$

By examining the generating bond pairs for the second-order invariants in this larger cell, it is seen that two of the invariants $I_{1,1}$ and $I_{1,2}$ have the same generating bond pairs as found in the second-order invariants for the primitive cell. The other two invariants $I_{1,6}$ and $I_{1,5}$ are generated by bond pairs that are farther apart than possible in the primitive cell. It should be noted that H bonds throughout the entire lattice are generated by the action of the space group projection operator on a single bond. However, because of periodicity, the *value* of the bond variables can be expressed as the value of a bond within the unit cell. That is why the action of a projection operator containing an infinite number of translation elements gives rise to the finite expressions in Eqs. (7)–(10). The presence of $I_{1,1}$ and $I_{1,2}$ in this larger cell illustrates an important fact: that invariants in small cells will also be found in larger cells. In addition, new invariants not possible in the small cell will be associated with the larger cell. From close inspection of the invariants, when evaluated for the H-bond configurations consistent with the ice rules, it is clear that some invariants are now linearly dependent on other invariants. For example, in Table I one can verify that

$$I_{1,2} = \frac{1}{3} I_{1,1}, \quad (11)$$

$$I_{1,5} = I_{1,6} + 2I_{1,2} = I_{1,6} + \frac{2}{3} I_{1,1}. \quad (12)$$

Using $I_{1,1}$ and $I_{1,6}$ as independent variables, we can write down an expression relating scalar physical quantities to

functions of the H-bond topology. Assuming a simple linear form, the energy of an H-bond isomer, as a function of the bond variables, can be written as

$$E(b_1, b_2, \dots, b_8) = E_0 + \alpha I_{1,6}, \quad (13)$$

where E_0 is a constant and α can be determined by fitting to energies, obtained from either experiment or calculation, of H-bond configurations. The linear dependence among invariants induced by the constraints of the ice rules exposes relationships that are often not otherwise obvious. Taking the $(\text{H}_2\text{O})_8$ cubic clusters as an example, the “dimers” that Belair and Francisco [42] counted turned out to be linearly related to the nearest-neighbor “dangling hydrogens” counter by McDonald *et al.* [37]. Finally, graph invariants made the relationship clear [41].

The idea of correlating the energy of an H-bond configuration of ice to features of the H-bond topology is not new, but has never been successfully implemented in the past. Long ago, Bjerrum [43] suggested that H bonds in ice break into two categories, depending on whether the non-hydrogen-bonded hydrogens are in a *trans* or *cis* arrangement—that is, whether they fall on opposite or the same sides of the H bond, as illustrated in Figs. 1 and 2. The presumed dominance of pairwise interactions has led to proposals that ice structures with the highest fraction of *trans* H bonds are the most stable [43], a notion that, if correct, would conflict with the proposed ferroelectric structure of ice XI, Fig. 2, in which three-quarters of the H bonds are *cis*. Also, as described below, another conflicting result is that both the lowest- and highest-energy configurations for a $2 \times 2 \times 2$ unit cell of ice VII contain no H bonds in the *trans* configuration. Nevertheless, the number of *trans* bonds is actually an example of an invariant and is useful for outlining our bootstrap strategy of invariants to larger unit cells. The *cis-trans* energy difference is a parameter that can be determined from small unit cells [44]. Electronic structure calculations could be performed on a small unit cell to calculate the *cis-trans* energy. Next, the *cis-trans* energy difference could be calculated for larger unit cells, for which these types of calculations are feasible, thus indicating whether

convergence to the large cell limit has been reached. Then the number of trans bonds could be used to extrapolate to even larger unit cells where it is not possible to do these calculations on the billions of possible H-bond arrangements needed for statistical simulations. If the relative number of *cis* and *trans* bonds did control the energy, then the energy of the billions of H-bond arrangements possible in a large cell would be known by counting the relative number of *cis* and *trans* H bonds in each of those configurations. While, as argued above, the number of *cis-trans* bonds is not sufficient to describe the H-bond energetics of ice, an analogous bootstrap strategy using graph invariants will prove successful.

Graph invariants provide a hierarchy of increasingly accurate approximations, with two independent routes for improving the description of scalar physical quantities. The first is determined by the number of bonds multiplied to generate an invariant—i.e., the order of the invariant polynomial in bond variables. Invariants can be constructed by projecting onto a single bond, a bond pair, a bond triplet, and so on corresponding to first-, second-, third-, and higher-order invariants, respectively. We have already demonstrated [38] how graphical techniques can be used to understand and predict physical properties of water clusters, finding that the expansion was well converged at second order. As will be described below, the energy of H-bond isomers for various unit cells of ice is also well described using second-order invariants. The second manner by which the invariant approximation could be improved is by including invariants generated by bond pairs separated by greater distances. As described above, invariants for a large unit cell, when compared to invariants from a smaller unit cell, can be divided into two groups: those invariants that were only present in the smaller unit cell and those invariants generated by bond pairs farther apart than possible in the smaller unit cell. Including invariants generated by bonds only possible in the larger unit cells would improve the approximation. As will be described below, acceptable convergence for the energy of H-bond isomers of ice only requires bond pairs that are nearest neighbors. This feature may no longer hold true when the theory is generalized to include charged or Bjerrum defects.

The proton-order and -disorder transitions in the various ice phases all share similar features. The underlying oxygen lattice is essentially unchanged between the disordered and ordered configurations. Hence, we neglect the small lattice parameter changes as the temperature changes. As indicated above, experiments on samples of H₂O and D₂O indicate a difference in the transition temperature of a few degrees. In experiments on ice Ih, the proton ordering transition occurs at 72 K for H₂O and 76 K for D₂O, a difference of 4 K [8,9]. A significant change in the transition temperature due to a change in mass is a sign that quantum effects are important. The small shift in the transition temperature indicates that quantum effects are negligible; thus, we use classical statistical mechanics for our calculations. Working within classical statistical mechanics, the partition function for ice can be written as a sum of contributions from the M symmetry-distinct local minima of the potential energy surface [38,39]. At sufficiently low temperature the classical procedure could be modified to include quantum effects—for example, by calculating the vibrational free energy quantum

mechanically. However, the use of classical statistical mechanics seems appropriate for H-bond-order- and -disorder transitions in ice.

Assuming the simplest linear dependence [45], the energy of an H-bond isomer as a function of the bond variables is written as

$$E(b_1, b_2, \dots) = E_0 + \sum_r \alpha_r J_r + \sum_{rs} \alpha_{rs} J_{rs} + \dots, \quad (14)$$

with the overall constant E_0 and the α coefficients to be determined either by comparison with experiment or, as we do in this work, by first-principles calculations. For our bootstrap strategy, we first determine the graph invariants for a small unit cell of ice from which a training set of isomers is chosen for DFT calculations which will determine the coefficients in the energy expression (14). Next, the graph invariants for a larger unit cell are determined. Each successively larger cell contains invariants that were already present in the smaller cell as well as new invariants involving bond combinations that are farther apart than possible in the small unit cell. A handful of isomers is chosen from the larger cell, DFT calculations are performed, and invariant parameters are refit to the energy expression. Enlarging of the unit cell is continued until the invariant parameters converge and new invariants become unimportant. The converged invariant parameters will then be used to evaluate the energy expression for the many H-bond isomers of a large simulation cell to generate statistical averages. Our results indicate there are other important features, besides *cis* and *trans* H bonds, which are required to appropriately link scalar physical properties to H-bond topology in ice. The use of graph invariants provides a systematic means to generate the full set of topological parameters, in the form of invariant polynomials of bond variables b_r , and organizing them in a hierarchy of increasingly accurate approximations [38,39]. In this work we only retain the leading-order—that is, second-order-invariants, which will be seen to provide an accurate description of the H-bond energetics of larger ice unit cells.

III. ICE VII/VIII

Our study of proton ordering phase transitions in ice begins with the well-characterized ice VII/VIII transition. The smallest unit cell we examined was a cubic 16-water-molecule unit cell of ice VII, two primitive unit cells on each side as shown in Fig. 5. The lattice constant used in the following calculations was $a=3.337$ Å, as determined by diffraction studies at 1.1 GPa and 263 K [28].

All first-order invariants for the $2 \times 2 \times 2$ cell were identically zero for reasons described in Sec. II. There are eight second-order graph invariants for this cell, which, when evaluated for the 52 symmetry-distinct H-bond isomers possible in this unit cell, enumerated using previously described methods [31,37,38], could be sorted into two groups. The first group contained two invariants which evaluated to the same constant for all H-bond configurations and the second group consisted of the remaining six invariants. The two invariants in the first group, $I_{1,1}$ and $I_{1,5}$, were generated by bond pairs that had at least one common vertex. $I_{1,1}$ was

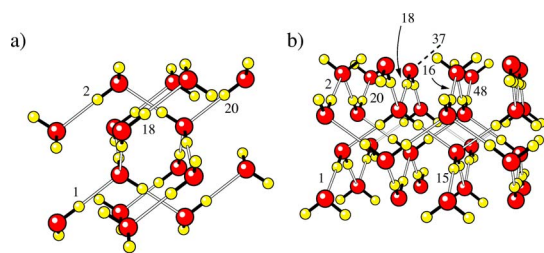


FIG. 5. (Color online) (a) An H-bond isomer of a 16-water-molecule unit cell of ice VII measuring two primitive unit cells on each side. Bonds representative of the three second-order graph invariants used to fit the DFT energies are shown, as further described in Table II. (b) The ground-state H-bond isomer of a 32-water-molecule unit cell of ice VII measuring $2\sqrt{2} \times 2\sqrt{2} \times 2$ primitive cells on each side corresponding to the experimentally determined ice VIII structure. Bond pairs representative of the second-order graph invariants, including bond pairs not possible in the smaller 16-water-molecule unit cell, used to fit the DFT energies are shown. Bond 37 connects to a water molecule in an adjoining cell.

generated from $\hat{G}(b, b_r)$, and $I_{1,5}$ is equivalent to invariant $I_{1,2}$ found in the smaller unit cells discussed in Sec. II. Due to the periodicity constraints and the ice rules, invariants may become linearly dependent on other invariants when evaluated for H-bond isomers. The second group contained three linearly independent invariants while the first group contained only one invariant. Since it is arbitrary which invariants are chosen to be the linearly independent set of invariants, we selected invariants based on geometrical features of the generating bond pairs such as whether the generating bond pairs belong to the same sublattice and minimum distance between bond pairs. Geometrical features of the invariants included in Eq. (14) are described in Fig. 5 and at the top of Table II.

Periodic DFT calculations were performed on all 52 enumerated H-bond configurations using the Car-Parrinello [46,47] method with the Becke-Lee-Yang-Parr gradient correction [48,49] to the local density approximation and Martins-Troullier norm-conserving pseudopotentials [50]. The electronic wave function was expanded in plane waves

TABLE II. Geometrical features and contribution to the description of the energy of H-bond isomers of the second-order graph invariants. Invariants 4–7 do not appear in the 16-water-molecule, $2 \times 2 \times 2$ unit cell of ice VII. The indices of the generating bond pair refer to Fig. 5. The distance associated with each bond pair is the distance between the closest vertices from each bond in an ideal structure before geometry optimization. The last three columns give the fitting coefficients for each of the invariants as used in Eq. (14) for the energy in units of $\text{kcal mol}^{-1} \text{water}^{-1}$.

Invariant	Generating bond pair	Distance (\AA)	Same lattice?	16-water-molecule (inv. 1–3)	32-water-molecule (inv. 1–7)	32-water-molecule (inv. 1–3)
1	1,20	2.89	N	0.0155118	0.0243047	0.0192577
2	1,18	2.89	Y	-0.0471626	-0.0657520	-0.0709555
3	1,2	2.89	N	0.0907482	0.1009400	0.1093980
4	1,48	5.53	N		0.01063060	
5	1,16	5.53	N		-0.00705523	
6	1,15	4.72	Y		-0.00248413	
7	1,37	4.72	Y		0.01210390	

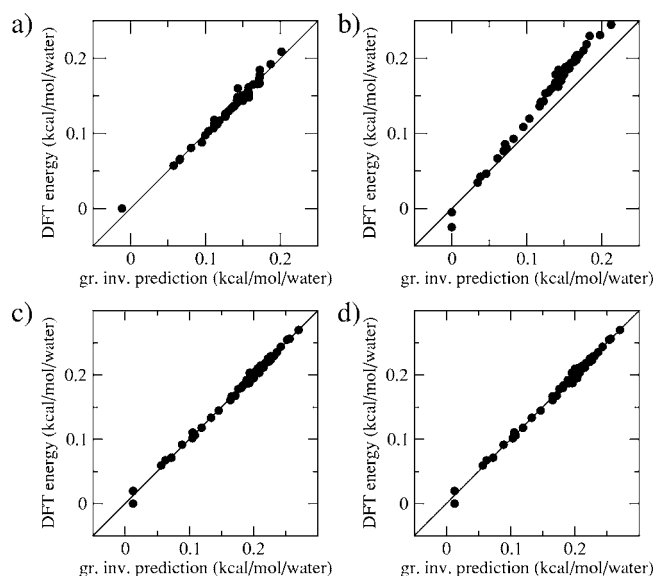


FIG. 6. (a) Graph-invariant fit to the energies of the 52 H-bond isomers of a 16-water-molecule unit cell of ice VII. (b) Calculated DFT energy of H-bond isomers of a 32-water-molecule ice VII cell plotted against energies predicted from graph-invariant parameters derived from the 16-water-molecule cell. (c) Graph-invariant fit, using second-order invariants whose generating bond pairs are farther apart than possible in the smaller 16-water-molecule unit cell, to the energies of the H-bond configurations for the 32-water-molecule unit cell. (d) Same as plot (c) except only invariants whose generating bond pairs exist in the smaller 16-water-molecule unit cell were fit to the energies. A line of slope unity is shown to indicate where points would lie for perfect agreement. Invariant coefficients for each of the three fits are listed in Table II.

up to a cutoff of 70 Ry. The Brillouin zone sampling was restricted to the Γ point. The dependence of energy on H-bond topology was well captured by an expression, Eq. (14), with second-order invariants as the leading term, as shown in Fig. 6(a). The DFT energy is plotted against a linear fit to the 52 energies using the first three invariants listed in Table II plus an overall constant. In Fig. 6, perfect agreement is indicated when points lie on the diagonal line.

Next, calculations were performed on a larger ice VII unit cell, measuring $2\sqrt{2} \times 2\sqrt{2} \times 2$ primitive cells on each side. As discussed above, in Sec. II, all invariants from the smaller cell were also found in the larger unit cell. All first-order invariants were algebraically zero. There were ten additional second-order graph invariants generated from bond pairs that were farther apart than possible in the smaller 16-water-molecule unit cell. DFT calculations were performed on 50 H-bond isomers chosen “semirandomly” from the 35 806 symmetry-distinct H-bond configurations possible in this unit cell [31,37,38]. From a prediction based on the graph-invariant parameters fit to the $2 \times 2 \times 2$ cell, we selected isomers that would cover the entire energy range, plus other isomers that would test whether the new invariants that appear for the larger $2\sqrt{2} \times 2\sqrt{2} \times 2$ cell are actually needed to fit the energy of the isomers for the larger cell. The energies of the 32-water-molecule unit cells are well predicted using invariants parameters obtained from calculations on the 16-water-molecule cell, shown in Fig. 6(b). However, there is a small systematic discrepancy in which the invariant prediction overestimates the energy differences in the 32-water-molecule cell. This discrepancy is actually not a consequence of requiring more invariant parameters for the larger cell but instead arises because the conditions under which the calculation is performed change with cell size. In the larger cell, there is more freedom for configurational relaxation and greater effective k -point sampling at the Γ point. Thus, the small discrepancy is actually an indication that we are nearing convergence of the graph-invariant parameters with respect to both unit-cell size and k -point sampling.

Of the 18 second-order invariants for the $2\sqrt{2} \times 2\sqrt{2} \times 2$ cell, eight invariants were linearly independent when evaluated for all H-bond configurations. A fit of the DFT energies incorporating invariants whose generating bond pairs were farther apart than possible in the smaller 16-water-molecule unit cell [Fig. 6(c)] yielded a fit just as good in quality as that obtained from only using invariants whose generating bond pairs existed in the smaller cell [Fig. 6(d)]. We conclude that the energy of the H-bond isomers is accurately described by invariants whose generating bond pair contain vertices that are nearest neighbors. Energy plotted as a function of the percent of *trans* H bonds is shown in Fig. 7. For both unit cells, the ground-state and highest-energy configurations contain no bonds that are *trans*. If the relative number of *trans* bonds was the only feature of the H-bond topology used to describe the energetics, those configurations would then be degenerate. Clearly, it is evident that additional features of the H-bond topology, exhibited by the graph invariants, are necessary to accurately describe the relative energetics of H-bond isomers of ice.

Using the improved invariant parameters and Eq. (14), we have a Hamiltonian describing the energy differences due to fluctuating H bonds in a large simulation cell. Rather than introducing possible uncertainty associated with further approximations, we obtained an essentially exact numerical solution for the thermal behavior governed by the H-bond Hamiltonian using the standard Metropolis Monte Carlo algorithm (e.g., Ref. [51]). When simulating our model at low temperatures, where the acceptance of trial moves is rare, we found that care in the choice of random number generator

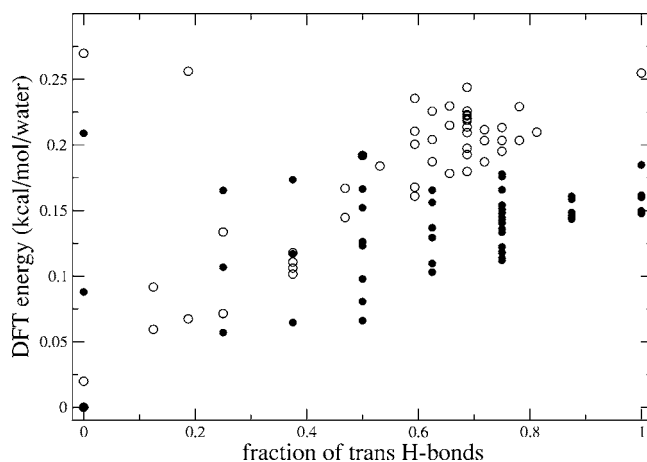


FIG. 7. Relative DFT energy of H-bond isomers of a 16-water-molecule (●) and 32-water-molecule (○) unit cell of ice VII plotted against fraction of *trans* bonds for each isomer. The lowest- and highest-energy isomers for both unit cells contain no H bonds in the *trans* configuration, thus indicating that features of the H-bond topologies other than *cis-trans* H bonds are important if physical properties are to be correctly described.

was required and that some random number generators produced artificial periodic excitations out of the ground state with a period lasting thousands of Monte Carlo passes. Since this behavior only occurred when excitations were rare, it actually had no effect on the statistical averages reported below. Nevertheless, we took care to find simulation conditions free of artificial periodic behavior. We found that the “Mersenne Twister” generator developed by Matsumoto and Nishimura [52] was not susceptible to the spurious behavior. The only nonstandard feature of our Monte Carlo algorithm is the generation of the trial moves, since our trial rearrangements of H bonds must not violate the ice rules. We use the algorithm invented by Rahman and Stillinger [53] for sampling H-bond configurations in ice. The Rahman-Stillinger idea is to randomly identify closed loops of H bonds. Flipping the entire loop of H bonds will preserve the number of outgoing and incoming bonds at each oxygen atom and will not “break” any water molecules, thereby preserving the ice rules. Recently, Rick and Haymet have generalized the Rahman-Stillinger idea to do off-lattice simulations of ice [54]. In their paper, one can find references to work where the ergodic nature of the Rahman-Stillinger loop algorithm was proved. In an approximation where the total dipole is a sum of bond dipoles, it is easily seen that closed loops do not change the total dipole moment of the system. However, as Rahman and Stillinger noted, loops that begin in one periodic simulation cell and terminate in another cell will change the dipole moment. We allow both types of moves because we want to sample all H-bond configurations, including ferroelectric and antiferroelectric configurations, and allow exact statistical simulations to identify the equilibrium properties of the system.

Metropolis Monte Carlo simulations were performed on a simulation cell measuring eight primitive cells on each side containing 1024 water molecules. A series of simulations were performed for both increasing and decreasing tempera-

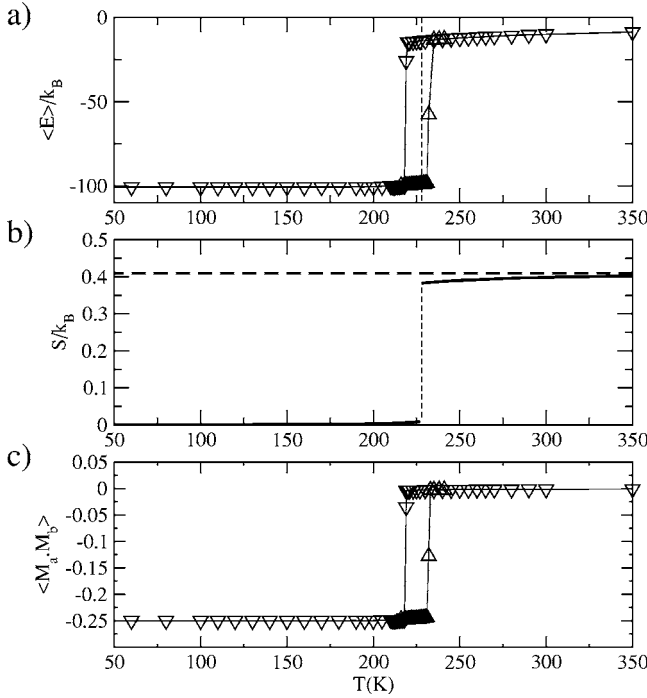


FIG. 8. (a) Average energy plotted as a function of temperature from Metropolis Monte Carlo simulations for large simulation cell of ice VII/VIII. Data are presented for series of Metropolis Monte Carlo runs ascending (Δ) and descending (∇) in temperature. The vertical line is located at the calculated transition temperature near 228 K. (b) Entropy plotted as a function of temperature. The horizontal line is the Pauling entropy for a fully disordered ice lattice subject to the ice rules. (c) Degree of antiferroelectric ordering of the ice VII sublattices as a function of temperature. \mathbf{M}_a and \mathbf{M}_b are the total dipoles, in units of bond dipoles, for the two independent sublattices.

tures. The initial structure for the increasing temperature simulations was that of the experimentally determined ice VIII structure. The final configuration for each simulation was always the initial configuration for the next simulation. The initial configuration for the series of simulations with decreasing temperature was an H-bond configuration equilibrated at an extremely high temperature, $\sim 10^7$ K.

The Monte Carlo simulations yield a prediction of a first-order phase transition near 228 K with significant hysteresis, as shown in Fig. 8(a). The transition temperature is calculated as the point of equal free energy [$\Delta A=0$ in Eq. (15)] between the two phases as determined by thermodynamic integration of the low-temperature proton ordered phase from 0 K and the high-temperature proton-disordered phase from infinite temperature:

$$\Delta A(T) = [E_H(T) - E_L(T)] - T[S_H(T) - S_L(T)], \quad (15)$$

$$S_H = S(\infty) - \int_T^\infty dT' \frac{C_V}{T'}, \quad (16)$$

$$S_L = \int_0^T dT' \frac{C_V}{T'}. \quad (17)$$

Since we neglect the effect of what is known to be a small change in the lattice constant with temperature, we do not include a pressure-volume term in the free energy. The constant $S(\infty)$ in Eq. (16) for the entropy of the high-temperature phase is the configurational entropy for a fully disordered ice phase subject to the ice rules which we take from the work of Nagle: $S(\infty) = Nk_B \ln(1.5069)$ [3]. Entropy as a function of temperature is plotted in Fig. 8(b). With decreasing temperature, 7% of the ideal entropy for a fully disorder ice phase is lost before the transition. The calculated entropy at the transition, 228 K, is 91% of the ideal configurational entropy associated with H-bond disordering compared with experimentally reported values of 83% for H_2O and 91% for D_2O [33].

Partial disordering below the transition is also observed in a plot of $\langle \mathbf{M}_a \cdot \mathbf{M}_b \rangle$ as a function of temperature, as shown in Fig. 8(c). \mathbf{M}_a and \mathbf{M}_b are the dipole moments, calculated using a bond dipole approximation, for each of the two independent sublattices, and $\langle \dots \rangle$ is an ensemble average. \mathbf{M}_a and \mathbf{M}_b are each normalized to $N\mu_{\text{H}_2\text{O}}$, where $\mu_{\text{H}_2\text{O}}$ is the dipole moment magnitude of one water molecule and N is the total number of waters in one system:

$$\mathbf{M}_x = \frac{1}{N\mu_{\text{H}_2\text{O}}} \sum_{i \in \text{sublattice } x} \boldsymbol{\mu}_i, \quad x = a, b. \quad (18)$$

At high temperatures, $\langle \mathbf{M}_a \cdot \mathbf{M}_b \rangle$ is zero corresponding to fully disordered ice VII. At low temperatures, antiferroelectrically ordered ice VIII is the stable phase with both sublattices oriented oppositely so that

$$\langle \mathbf{M}_a \cdot \mathbf{M}_b \rangle = \frac{[(-N/2)\mu_{\text{H}_2\text{O}}][(N/2)\mu_{\text{H}_2\text{O}}]}{|N\mu_{\text{H}_2\text{O}}|^2} = -\frac{1}{4}. \quad (19)$$

Figure 8(c) indicates that the degree of pretransitional alignment and post-transitional disorder in $\langle \mathbf{M}_a \cdot \mathbf{M}_b \rangle$ is small.

Despite the challenge posed by small energy variation among H-bond isomers, our results qualitatively match the observed features of the ice VII/III phase transition in several respects: (1) the calculated ground state is the known ice VIII antiferroelectric structure [31], (2) the transition temperature of 228 K is similar to the experimental transition point measured in the range 263–274 [28,33], and (3) the detectable partial ordering above the transition and partial disordering below the transition, as measured by the entropy at the transition, is in agreement with experiment.

IV. ICE Ih/XI

Having calibrated our methods with the ice VII/III transition, we now turn to ice Ih/XI, which is not as well characterized experimentally. Given the degree of controversy surrounding the Ih/XI transition and the small energy differences, we attempted to gauge how sensitive the calculated energy differences were to the level of theoretical treatment. We performed DFT calculations for ice Ih using three

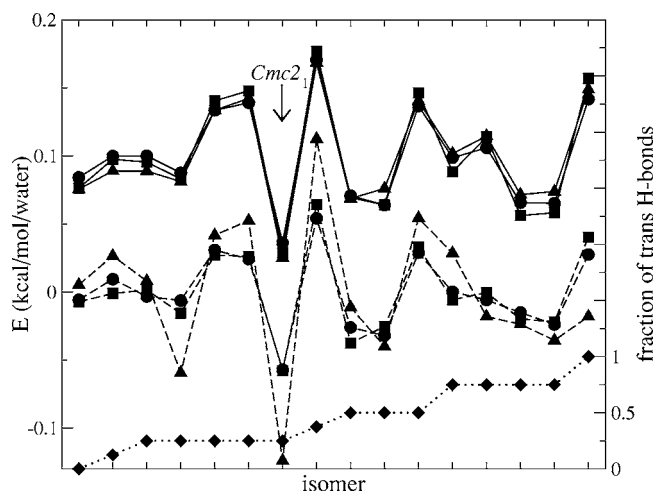


FIG. 9. Relative energy of H-bond isomers calculated by periodic electronic DFT methods for 16 isomers of an eight-water-molecule orthorhombic unit cell listed in order of increasing fraction of *trans* H bonds. The lowest graph (dotted lines) gives the fraction of *trans* H bonds associated with each isomer. The energy of the H-bond isomers was calculated using the programs (●, ○) CPMD, (■, □) DMOI, and (▲, △) CASTEP. Solid lines: energy of H-bond isomers before geometry optimization. Dashed lines: energies after optimization of the molecular coordinates and for the CASTEP results cell dimensions as well. The six energy data sets, optimized and unoptimized, are plotted with their average taken as the zero of energy to facilitate comparison of the relative energies of the isomers. For clarity, the $Cmc2_1$ isomer is noted and the optimized data sets are shifted by 0.06 kcal/mol.

different combinations of density functionals and basis sets for two smaller unit cells of ice Ih, an orthorhombic unit cell containing eight water molecules [44] and a hexagonal cell with 12 water molecules. The lattice constants for all unit cells of ice Ih used in the following calculations are tabulated in an earlier report [40]. The number of symmetry-distinct H-bond isomers consistent with the ice rules and lattice periodicity is 16 and 14, respectively [39].

Three separate methods of calculation were employed to check the consistency of electronic density functional theory in describing the energetics of H-bond isomers. The Car-Parrinello [46,47] method was used as previously described. The Becke-Lee-Yang-Parr (BLYP) [48,49] functional using numerical basis sets was implemented within the DMOL program [55]. The CASTEP program [56] was used with the Perdew-Wang 1991 (PW91) functional [57–59] and a plane-wave basis. The different density functionals, basis sets, and programs agree quite well when applied to starting configurations (Fig. 9 for the 16-water-molecule orthorhombic unit cell and Fig. 10 for the 12-water-molecule hexagonal unit cell), for which the cell dimensions and molecular geometries for each isomer are exactly the same. Moreover, each method yields the $Cmc2_1$ structure as the lowest-energy isomer. The isomers are arranged in Figs. 9 and 10 in order of increasing fraction of *trans* H bonds, and it is once again apparent that this feature does not predict their relative energies.

After comparing energies from different methods calculated for exactly the same geometries, we subsequently opti-

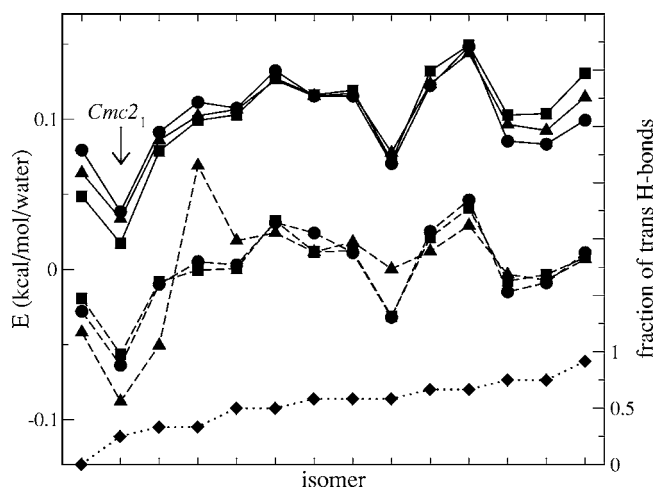


FIG. 10. Relative energy of H-bond isomers calculated by periodic electronic DFT methods for 14 isomers of a 12-water-molecule hexagonal unit cell listed in order of increasing fraction of *trans* H bonds. The lowest graph (dotted lines) gives the fraction of *trans* H bonds associated with each isomer. The energy of the H-bond isomers was calculated using the programs (●, ○) CPMD, (■, □) DMOI, and (▲, △) CASTEP. Solid lines: energy of H-bond isomers before geometry optimization. Dashed lines: energies after optimization of the molecular coordinates and, for the CASTEP results, cell dimensions as well. The six energy data sets, optimized and unoptimized, are plotted with their average taken as the zero of energy to facilitate comparison of the relative energies of the isomers. For clarity, the $Cmc2_1$ isomer is noted and the optimized data sets are shifted by 0.06 kcal/mol.

mized geometries within the capabilities of each method. For two of the methods, CPMD and DMOL, the atomic positions were optimized with cell dimensions fixed. Those two cases are in very good agreement. In the third method, CASTEP, the cell dimensions were optimized as well and, as would be expected, this case deviates further from the other two. As shown in Figs. 9 and 10, the overall trends do not depend on the choice of density functional or the optimization method. The lowest-energy isomer is the $Cmc2_1$ ferroelectric structure in each case. Similar comparisons from calculations using empirical water potentials indicated that the relative energetics of H-bond isomers differed by an order of magnitude among the models and none had identified the $Cmc2_1$ structure as the ground state [36]. While many commonly used empirical potentials do not give a reliable description of H-bond energetics in ice, DFT calculations provide a robust description.

As discussed above, the *ab* puckered sheets of the $Cmc2_1$ structure have a net polarization. The polarization alternates from sheet to sheet, making the ice XI structure antiferroelectric in the *ab* direction. Thus, the puckered sheets are slightly displaced in the direction of the polarization, as shown in Fig. 11, by a magnitude of $\epsilon/2$, where ϵ is the relative displacement of two adjacent layers. Using the optimized geometry of the 12-water-molecule $Cmc2_1$ structure, obtained using the Car-Parrinello [46,47] method as described above, we calculated the distance between the center of mass for each of the *ab* layers. The calculated value $\epsilon=0.11 \text{ \AA}$ is in agreement with the experimentally determined value $\epsilon=0.12 \text{ \AA}$ [13].

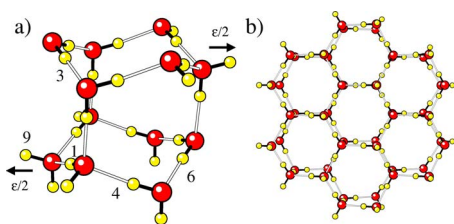


FIG. 11. (Color online) (a) An H-bond isomer of a 12-water-molecule primitive unit cell of ice Ih. Bonds representative of the three second-order graph invariants used to fit the DFT energies are shown, as further described in Table III. All bonds used to generate second-order invariants, used to describe energy differences for H-bond fluctuations in a large simulation cell, lie perpendicular to the c axis and are referred to as ab bonds. (b) An H-bond isomer of a 48-water-molecule unit cell of ice Ih measuring $2 \times 2 \times 1$ primitive cells on each side. Both H-bond isomers shown are the lowest-energy isomer for each unit cell in agreement with the experimentally proposed ferroelectric, space group $Cmc2_1$, ice XI structure. Arrows indicate the direction of the relative displacement $\epsilon/2$ of the ab layers which are oppositely polarized.

Similar to ice VII, all first-order invariants for both the 12-water-molecule hexagonal and eight-water-molecule orthorhombic unit cell were identically zero. Application of the projection operator for the totally symmetric representation on bond pairs in the 12-water hexagonal unit cell resulted in 13 second-order invariants for which five were linearly independent when evaluated for the enumerated H-bond configurations. Periodic DFT calculations using the Car-Parrinello [46,47] method, as described above, were performed on all H-bond isomers. A good description of the energetics was obtainable using only three invariant parameters, shown in Table III. The invariants listed in Table III represent a set of linearly independent invariants from among those for which the generating bond pairs are no farther apart than one nearest-neighbor distance. Since linear dependences exist among the invariants when evaluated for configurations that satisfy the ice rules, the choice of a set of independent parameters is arbitrary. Even though Table III only includes second-order invariants generated from pairs in the ab puckered sheets, the configuration of H bonds in the c direction is effectively included because these invariants are linearly dependent on those listed in Table III.

In the case of the eight-water-molecule orthorhombic unit cell, 16 second-order invariants exist for which six were linearly independent when evaluated for all enumerated H-bond

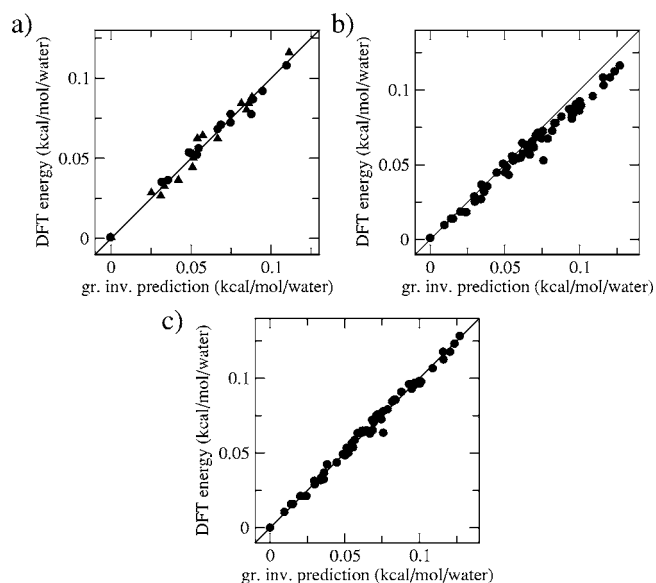


FIG. 12. (a) Graph-invariant fit to the energies of the 14 H-bond isomers of a 12-water-molecule hexagonal (\bullet) unit cell and the 16 H-bond isomers of an eight-water-molecule orthorhombic (\blacktriangle) unit cell of ice Ih. (b) Calculated DFT energy of H-bond isomers of a 48-water-molecule hexagonal ice Ih unit cell plotted against energies predicted from graph-invariant parameters derived from the small unit cells. (c) Graph-invariant fit to the energies of the 63 “semirandomly” chosen H-bond isomers of a 48-water-molecule hexagonal unit cell of ice Ih. A line of slope unity is shown to indicate where points would lie for perfect agreement.

configurations. The energy of the H-bond isomers was well described using invariants generated by the same three bond pairs as those that generated the invariants used to predict the energy of the 12-water-molecule hexagonal unit cell, Table III. The generating bond pairs for the invariants used to describe the energies of H-bond isomers in both unit cells are shown in Fig. 11. A combined fit of the DFT energies for both types of unit cells, hexagonal and orthorhombic, plotted against the predicted values using three invariant parameters is shown in Fig. 12.

Next, periodic DFT calculations were performed on a larger hexagonal unit cell, containing 48 water molecules, measuring $2 \times 2 \times 1$ primitive cells on each side. In order to evaluate the convergence of the invariants achieved in the small unit cells, the predicted energies of 63 H-bond configurations, chosen from the 836 0361 symmetry-distinct H-bond isomers possible in the larger unit cell [31,37,38], were com-

TABLE III. Geometrical features and contribution to the description of the energy of H-bond isomers of the second-order graph invariants. The indices of the generating bond pair refer to the H bonds shown in Fig. 11. The H bonds can be described as either lying parallel, c bonds, or perpendicular, ab bonds, to the c axis. The last four columns give the fitting coefficients for each of the invariants as used in Eq. (14) for the energy in units of $\text{kcal mol}^{-1} \text{water}^{-1}$.

Invariant	Generating bond pair	Bond type	12-water-molecule hex-($1 \times 1 \times 1$)	16-water-molecule orth-($2 \times 1 \times 1$)	12 and 16-water-molecule combined fit	48-water-molecule hex-($2 \times 2 \times 1$)
1	1,3	(ab),(ab)	0.0288485	0.0249965	0.0267952	0.0250812
2	4,9	(ab),(ab)	-0.0789488	-0.0775161	-0.0777339	-0.0952566
3	1,6	(ab),(ab)	0.0346155	0.0416369	0.0359921	0.0481123

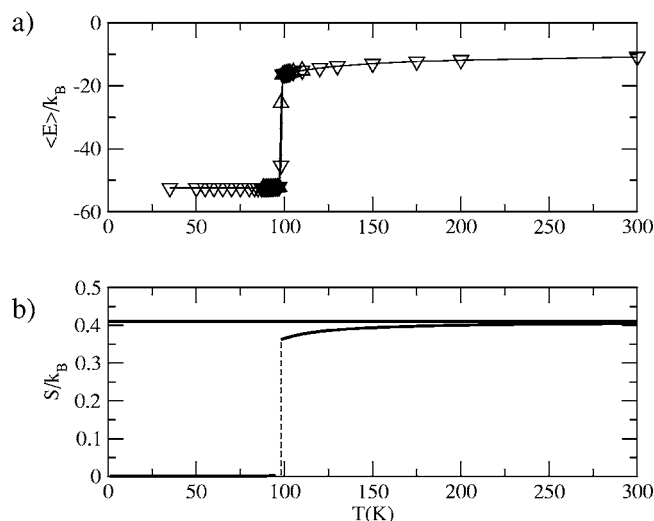


FIG. 13. (a) Average energy plotted as a function of temperature from Metropolis Monte Carlo simulations of a large simulation cell of ice Ih. Data are presented for series of Metropolis Monte Carlo runs ascending (Δ) and descending (∇) in temperature. (b) Entropy plotted as a function of temperature. The horizontal line is the Pauling entropy $k_B \ln \frac{3}{2}$ for a fully disordered ice lattice.

pared to the actual DFT energy, shown in Fig. 12. The 63 configurations for the $2 \times 2 \times 1$ cell were “semirandomly” chosen, as described in Sec. III, to provide coverage of the entire range of energies and test whether new invariants arising from the larger cell were required to describe the energetics. The predictions from the small cells do a good job at predicting the energies of the large cell isomers, even better than when compared to the small cell predictions of ice VII described above. Again, the small deviation can be accounted for by the additional freedom for geometrical relaxation and more effective k -point sampling at the Γ point in the larger cell. Similar to ice VII, we only require graph invariants generated by nearest-neighbor bond pairs to describe the energy differences due to the numerous H-bond configurations in a large simulation cell. By refitting the invariant coefficients to the large cell energies, we are able to, with Eq. (14), calculate the energy differences arising from the various H-bond configurations in Metropolis Monte Carlo simulations of a large ice Ih system.

Monte Carlo simulations of ice Ih were performed, following the same procedure for that of the ice VII simulations, using an orthorhombic cell measuring $7 \times 4 \times 4$ primitive cells on each side containing 896 water molecules. The average energy as a function of temperature indicates that a first-order transition to the low-temperature proton-ordered structure occurs near 98 K. The structure of the low-temperature phase is that of the experimentally proposed ferroelectric $Cmc2_1$ structure, shown in Fig. 2(c). The system exhibits negligible hysteresis, unlike that observed in the VII/VIII transition. Entropy as a function of temperature, shown in Fig. 13, indicates that as ice Ih is cooled, the system loses 11% of its configurational entropy before the transition, in agreement with pretransitional effects seen calorimetrically [9] and in diffraction studies [16]. Only 1% of the configurational entropy for an ideal ice phase is lost below

the transition, resulting in 88% of the ideal entropy lost at the transition.

V. DISCUSSION

In this work, we have presented the results of statistical simulations used to predict the proton-order and -disorder phase transition for two different ice systems, ices Ih/XI and VII/VIII. Using an analytic technique, graph invariants, we have illustrated how features of the H-bond topology can be linked to scalar physical properties, in this case energy, and used to extrapolate data taken from calculations on small units cells to calculate properties for simulation cells large enough to approach the thermodynamic limit. Our results indicate that invariants generated by pairs of bonds, whose closest-lying vertices are nearest neighbors, are appropriate to describing the energies of the numerous H-bond isomers possible in a large unit cell. Because the H-bond topology is highly constrained by the ice rules and periodic boundary conditions, as expressed by the linear dependence among graph invariants discussed in Sec. II, the correlations included by this procedure are of longer range.

The energy differences between the H-bond isomers in proton-disordered phases of ice are quite small, indicating that careful checking of our theoretical methods is needed. We have shown that electronic structure DFT methods are capable of describing the subtle energy differences between the various H-bond isomers possible in a given unit cell. We first validated our methods by predicting the proton ordering phase transition for the ice VII/VIII system. Our results yielded a transition to H-bond-ordered ice VIII near 228 K which is in qualitative agreement with the experimental transition temperatures 263–274 K [28,33]. We then reported on results from simulations of the ice Ih/XI phase which predicted that a transition should occur near 98 K to the proposed ground state. This is in good agreement with the observed transition at 72 K and 76 K for samples of D_2O . The functionals and optimization methods explored in this work correctly identified the ice VIII ground state from among the configurations possible in ice VII. The fact that our calculations yield a transition temperature close to the experimental results indicates that the energy spectrum of the H-bond isomers, not just the ground state, is described by our methods. The quality of the results for ice VII/VIII provide some calibration of our calculations for ice Ih/XI. In this case, three different combinations of electronic density functionals, basis sets, and optimization methods yielded a similar energy spectrum of the isomers. Our results for ice Ih/XI provide support for the interpretation of experimental observations as a transition to a ferroelectric $Cmc2_1$ structure. However, better experimental characterization of the low-temperature phase and close comparison with theory are certainly needed in the future. We have also validated our methods by successfully predicting the proton ordering phase transition of ice III to metastable ice IX [60,61]. The low-temperature proton-ordered structures of ices V and VI, which are stable at pressures intermediate to ices Ih and VII, have yet to be confirmed experimentally. In another work, we have predicted the transition to a new H-bond-ordered phase with the

underlying oxygen lattice of ice VI [60,62]. Those results indicate that a proton ordering transition should occur near 108 K to a ferroelectric phase.

This work has described the success of correlating features of the H-bond topology to scalar physical quantities in order to predict thermodynamic features of the ice phases. Avenues of future work include the prediction of other proton ordering phase transitions in ice and the effect of electric fields. It is also of interest to include the effect of defects, such as the Bjerrum D and L or ionic defects, on the description of physical properties of ice. Studies of an eight-water-molecule cluster [41] have shown that graph invariants accurately describe the change in physical properties when a defect is introduced (replacement of a water by a hydroxyl radical in that case). With an appropriate description of defects in ice, the mobility of defects throughout the disordered ice lattice, and hence the mechanism of H-bond order

and disorder in ice, could be studied. Further understanding of the relationship between defects and H-bond topology is required to gain insight into the dielectric behavior of ice. The combination of analytical and computational tools described in this work is one promising avenue for tackling these problems.

ACKNOWLEDGMENTS

C.K. and S.J.S. acknowledge NSF Grant No. CHE-0109243 for supporting this work and the Ohio Supercomputer Center for resources needed to perform the calculations reported here. T.K.H. is grateful for support from the Wenner-Gren Foundations. L.P.O. acknowledges the Swedish Research Council (VR) for financial support and the Swedish Supercomputer Centers (SNAC) for computational resources.

-
- [1] L. Pauling, *J. Am. Chem. Soc.* **57**, 2680 (1935).
 [2] W. F. Giauque and J. W. Stout, *J. Am. Chem. Soc.* **58**, 1144 (1936).
 [3] J. F. Nagle, *J. Math. Phys.* **7**, 1484 (1966).
 [4] H. Suga, *Thermochim. Acta* **300**, 117 (1997).
 [5] G. P. Johari and E. Whalley, *J. Chem. Phys.* **75**, 1333 (1981).
 [6] S. Kawada and J. Niinuma, *J. Phys. Soc. Jpn.* **43**, 715 (1977).
 [7] S. Kawada, *J. Phys. Soc. Jpn.* **44**, 1881 (1978).
 [8] S. Kawada, *J. Phys. Soc. Jpn.* **32**, 1442 (1972).
 [9] Y. Tajima, T. Matsuo, and H. Suga, *Nature (London)* **299**, 810 (1982).
 [10] H. Fukazawa, S. Mae, S. Ikeda, and O. Watanabe, *Chem. Phys. Lett.* **294**, 554 (1998).
 [11] Y. Wang, J. C. Li, A. I. Kolesnikov, S. Parker, and S. J. Johnsen, *Physica B* **276–278**, 282 (2000).
 [12] A. D. Fortes, I. G. Wood, D. Grigoriev, M. Alfredsson, S. Kipfstuhl, K. S. Knight, and R. I. Smith, *J. Chem. Phys.* **120**, 11376 (2004).
 [13] R. Howe and R. W. Whitworth, *J. Chem. Phys.* **90**, 4450 (1989).
 [14] S. M. Jackson, V. M. Nield, R. W. Whitworth, M. Oguro, and C. C. Wilson, *J. Phys. Chem. B* **101**, 6142 (1997).
 [15] A. J. Leadbetter, R. C. Ward, J. W. Clark, P. A. Tucker, T. Matsuo, and H. Suga, *J. Chem. Phys.* **82**, 424 (1985).
 [16] C. M. B. Line and R. W. Whitworth, *J. Chem. Phys.* **104**, 10008 (1996).
 [17] S. M. Jackson and R. W. Whitworth, *J. Chem. Phys.* **103**, 7647 (1995).
 [18] S. M. Jackson and R. W. Whitworth, *J. Phys. Chem. B* **101**, 6177 (1997).
 [19] M. J. Iedema, M. J. Dresser, D. L. Doering, J. B. Rowland, W. P. Hess, A. A. Tsekouras, and J. P. Cowin, *J. Phys. Chem. B* **102**, 9203 (1998).
 [20] G. P. Johari, *J. Chem. Phys.* **109**, 9543 (1998).
 [21] M. Kunst and J. M. Warman, *J. Chem. Phys.* **87**, 4093 (1983).
 [22] P. J. Wooldridge and P. Devlin, *J. Chem. Phys.* **88**, 3086 (1988).
 [23] J. P. Cowin, A. A. Tsekouras, M. J. Iedema, K. Wu, and G. B. Ellison, *Nature (London)* **398**, 405 (1999).
 [24] M. Tyagi and S. S. N. Murthy, *J. Phys. Chem. A* **106**, 5072 (2002).
 [25] P. W. Bridgman, *J. Phys. Chem.* **5**, 964 (1937).
 [26] B. Kamb and B. L. Davis, *Proc. Natl. Acad. Sci. U.S.A.* **52**, 1433 (1964).
 [27] G. E. Walrafen, M. Abebe, F. A. Mauer, S. Block, G. J. Piermarini, and R. Munro, *J. Chem. Phys.* **77**, 2166 (1982).
 [28] W. F. Kuhs, J. L. Finney, C. Vettier, and D. V. Bliss, *J. Chem. Phys.* **81**, 3612 (1984).
 [29] R. J. Nelmes, J. S. Loveday, R. M. Wilson, J. M. Besson, P. Pruzan, S. Klotz, G. Hamel, and S. Hull, *Phys. Rev. Lett.* **71**, 1192 (1993).
 [30] L. Ojamäe, K. Hermansson, R. Dovesi, C. Roetti, and V. R. Saunders, *J. Chem. Phys.* **100**, 2128 (1994).
 [31] J.-L. Kuo and M. L. Klein, *J. Phys. Chem. B* **108**, 19634 (2004).
 [32] E. Whalley, D. W. Davidson, and J. B. R. Heath, *J. Chem. Phys.* **45**, 3976 (1966).
 [33] G. P. Johari, A. Lavergne, and E. Whalley, *J. Chem. Phys.* **61**, 4292 (1974); **73**, 4150(E) (1980).
 [34] P. Pruzan, J. C. Chervin, and B. Canny, *J. Chem. Phys.* **97**, 718 (1992).
 [35] C. W. F. T. Pistorius, E. Rapoport, and J. B. Clark, *J. Chem. Phys.* **48**, 5509 (1968).
 [36] V. Buch, P. Sandler, and J. Sadlej, *J. Phys. Chem. B* **102**, 8641 (1998).
 [37] S. McDonald, L. Ojamäe, and S. J. Singer, *J. Phys. Chem. A* **102**, 2824 (1998).
 [38] J.-L. Kuo, J. V. Coe, S. J. Singer, Y. B. Band, and L. Ojamäe, *J. Chem. Phys.* **114**, 2527 (2001).
 [39] J.-L. Kuo and S. J. Singer, *Phys. Rev. E* **67**, 016114 (2003).
 [40] S. J. Singer, J.-L. Kuo, T. K. Hirsch, C. Knight, L. Ojamäe, and M. L. Klein, *Phys. Rev. Lett.* **94**, 135701 (2005).
 [41] S. D. Belair, J. S. Francisco, and S. J. Singer, *Phys. Rev. A* **71**, 013204 (2005).
 [42] S. D. Belair and J. S. Francisco, *Phys. Rev. A* **67**, 063206 (2003).

- [43] N. Bjerrum, *Science* **115**, 386 (1952).
- [44] T. K. Hirsch and L. Ojamäe, *J. Phys. Chem. B* **108**, 15856 (2004).
- [45] Including high-order invariants could be regarded as implementing a more complicated functional form.
- [46] R. Car and M. Parrinello, *Phys. Rev. Lett.* **55**, 2471 (1985).
- [47] R. Car and M. Parrinello, in *Simple Molecular Systems Very High Density*, edited by A. Polian, P. Loubeyre, and N. Boccara, Vol. 186 of *NATO Advanced Study Institute Ser. B: Physics* (Plenum, New York, 1989), p. 455.
- [48] A. D. Becke, *Phys. Rev. A* **38**, 3098 (1988).
- [49] C. Lee, W. Yang, and R. G. Parr, *Phys. Rev. B* **37**, 785 (1988).
- [50] N. Troullier and J. L. Martins, *Phys. Rev. B* **43**, 1993 (1991).
- [51] *Monte Carlo Methods in Statistical Physics*, 2nd ed., edited by K. Binder, Vol. 7 of *Topics in Current Physics* (Springer, New York, 1986).
- [52] M. Matsumoto and T. Nishimura, *ACM Trans. Model. Comput. Simul.* **8**, 3 (1998).
- [53] A. Rahman and F. H. Stillinger, *J. Chem. Phys.* **57**, 4009 (1972).
- [54] S. W. Rick and A. D. J. Haymet, *J. Chem. Phys.* **118**, 9291 (2003).
- [55] B. Delley, *J. Chem. Phys.* **92**, 508 (1990).
- [56] V. Milman, B. Winkler, J. A. White, C. J. Pickard, M. C. Payne, E. V. Akhmatkaya, and R. H. Nobes, *Int. J. Quantum Chem.* **77**, 895 (2000).
- [57] J. P. Perdew and Y. Wang, *Phys. Rev. B* **33**, R8800 (1986).
- [58] J. P. Perdew, in *Electronic Structure of Solids, '91*, edited by P. Ziesche and H. Eschrig, Wissenschaftsbereich Theoretische Physik (Akademie Verlag, Berlin, 1991), p. 11.
- [59] J. P. Perdew and Y. Wang, *Phys. Rev. B* **45**, 13244 (1992).
- [60] J.-L. Kuo, *Phys. Chem. Chem. Phys.* **7**, 3733 (2005).
- [61] C. Knight and S. J. Singer (unpublished).
- [62] C. Knight and S. J. Singer, *J. Phys. Chem. B* **109**, 21040 (2005).